

Turbulence Energetics in an Inclined Interface Richtmyer-Meshkov Instability

Akshay Subramaniam

Department of Aeronautics & Astronautics,
Stanford University
496 Lomita Mall, Stanford, CA, USA 94305
akshays@stanford.edu

Sanjiva K. Lele

Department of Aeronautics & Astronautics,
Stanford University
496 Lomita Mall, Stanford, CA, USA 94305
lele@stanford.edu

ABSTRACT

The interaction of a Mach 1.55 shockwave with a nominally inclined interface between N_2 and CO_2 is considered. Unlike the classical Richtmyer-Meshkov problem, the interface evolution is non-linear from early time and large highly correlated vortical structures are observed even after reshock. Simulations target the experiment of McFarland *et al.* (2014). Simulations are performed using high-order spectral-like numerics (Lele, 1992). Results from multiple grid resolutions up to 4 billion grid points establish grid insensitivity of important physical quantities. Comparisons to the experiments show that the simulations adequately capture the physics of the problem. Analysis of the simulation data based on variable density turbulence equations in the Favre averaged and filtered form is presented. Statistics of unclosed terms in the averaged and filtered variable density equations are presented with a focus on the energy dynamics. It is observed that the inhomogeneity in the problem results in a non-monotonic return to isotropy of the Reynolds stresses post reshock and that compressibility effects are strong long after reshock due to large scale pressure-dilatation correlation. Binning the kinetic energy into logarithmically spaced bins in wavenumber space shows a k^{-2} scaling of the energy spectrum post reshock instead of the standard $k^{-5/3}$ power law.

INTRODUCTION

The Richtmyer-Meshkov (RM) instability is a hydrodynamic instability caused due to the interaction of a shockwave with a material interface. Akin to Rayleigh-Taylor instability where gravity acts to produce vorticity at the material interface, in RM flows, baroclinic vorticity generation deposits vorticity on the material interface when there is a misalignment of the pressure and density gradients rendering the interface unstable to a broad wavenumber range of disturbances.

The RM instability is an important phenomenon in many engineering and science applications involving material mixing. It is important in supersonic combustion as an enhancer of mixing between fuel and oxidizer. It is important in astrophysical applications, especially in the physics of supernovae to explain the lack of stratification in supernova remnants. It is also a major roadblock in achieving sustained fusion in Inertial Confinement Fusion (ICF) and can cause reduced yield and potentially inhibit startup.

PROBLEM SETUP

In this work, we simulate the RM instability arising from the interaction of a shockwave with a material interface that has a mean inclination with respect to the shockwave. Simulations presented here target the experiment in McFarland *et al.* (2014). Figure 1 shows a schematic of the problem setup. A material interface between N_2 and CO_2 with a $\theta = 60^\circ$ mean inclination is initialized just downstream of a Mach 1.55 shockwave in N_2 . Small perturbations on top of the mean inclination are added based on the experimentally measured profiles. A detailed description of the initial interface description is given in McFarland *et al.* (2014). Figure 2

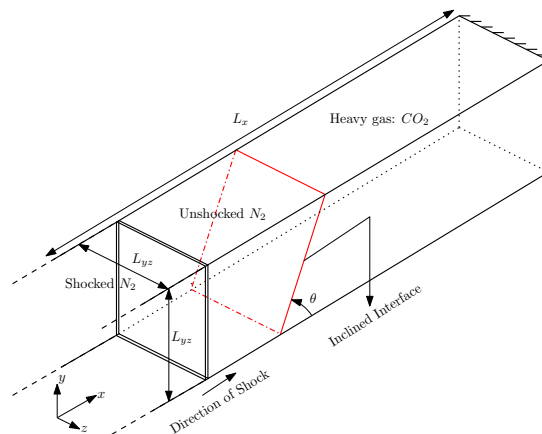


Figure 1: A schematic of the problem setup. Domain extends from 68.58cm to 256.46cm in x , 0cm to 11.43cm in y and -1.429cm to 1.429cm in z .

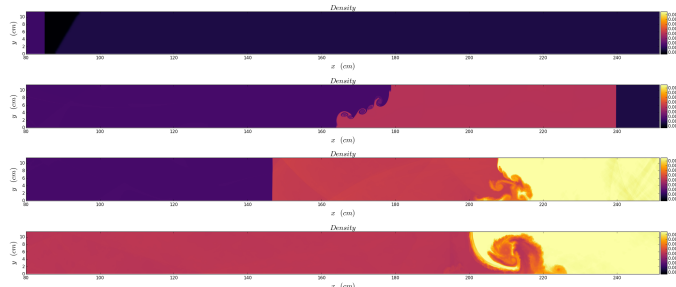


Figure 2: Plot of the z averaged density field at $t = 0\text{ms}$, 3.5ms , 7.2ms and 12ms from top to bottom.

shows the density field at different times that visualizes the shock and interface.

The shocktube in the experiment has a square cross section with side 11.43cm . In the simulations (see Figure 1), we idealize the spanwise (z) direction to be homogeneous (and periodic) by neglecting the wall effects in that direction and simulate a quarter of the cross section in the z direction. In the y direction, we use free-slip wall boundary conditions that capture the inviscid blocking effect of the wall but not the viscous boundary layers. Their effect is expected to be small over the time scales of inertially driven bulk instability arising in this problem. At the left x boundary, we use a sponge layer to absorb any waves that may reach this boundary and at the right x boundary is a wall.

NUMERICAL METHOD

The full compressible multi-species Navier-Stokes equations are solved in conservative form. Pressure and thermal equilibrium

between the two species is assumed at every point in the domain that gives a mixture rule. The equations solved here are the same as in Tritschler *et al.* (2014).

Simulations are performed using the Miranda code developed at Lawrence Livermore National Laboratory (LLNL). The equations are discretized using a 10th order compact finite difference scheme (Lele, 1992) in space. Time integration is performed using a 4th order 5 stage Runge-Kutta scheme (Kennedy *et al.*, 2000). Numerical regularization for shock and interface capturing is done using the LAD scheme (Cook, 2007; Kawai & Lele, 2008). The main idea behind the LAD scheme is to add artificial viscous stresses, conductive fluxes and diffusive fluxes that are localized to regions of discontinuities in order to add the minimal required amount of dissipation. The LAD scheme explicitly adds dissipation to capture shocks, interfaces and sub-scale features and acts like a sub-grid model. This allows for explicit computation of the energy dissipation introduced by the LAD scheme and can be accounted for in energy budgets unlike in other numerical methods where dissipation is added implicitly through upwinding. The grid used is an isotropic cartesian grid. The different grids used are listed in Table 1.

Table 1: Different grids used for the simulations. N is the number of points in the transverse direction.

N	Label	Grid	Final time
128	A	$2048 \times 128 \times 32$	12ms
256	B	$4096 \times 256 \times 64$	12ms
512	C	$8192 \times 512 \times 128$	12ms
1024	D	$16384 \times 1024 \times 256$	3.5ms

RESULTS

In the inclined interface RM instability, the interface is rendered unstable when the shock first impinges on the interface due to baroclinic torque. Due to the inhomogeneity in the transverse direction, the net circulation is non-zero and large rollers are formed as the interface evolves. The transmitted shock wave reflects from the end wall and a second interaction of the interface with a shock (or reshock) occurs at $t \approx 5.5ms$. Post reshock, the net circulation is opposite to the pre reshock value since the reflected shock is propagating in the opposite direction as the initial shockwave. This causes a large scale overturning of the interface. The second shock interaction also adds baroclinic vorticity at much smaller scales and the mixing region becomes much more turbulent. Subsequent weaker shocks and rarefactions interacting with the interface cause further modifications of the turbulent structures in the mixing region.

Comparison with experiments

To validate the simulations, we compare the simulation results to the results of McFarland *et al.* (2014). Figure 3 shows the evolution of the mixed width defined as $\delta = 4 \int \langle Y_{CO_2} \rangle_{yz} (1 - \langle Y_{CO_2} \rangle_{yz}) dx$ where $\langle \cdot \rangle_{yz}$ indicates average in the y and z directions. We see that the mixed width converges with increasing resolution and comparison with the experimental results is very good. Since the instability is driven by baroclinic vorticity deposited by the shock, the total circulation and the positive and negative contributions to it are good quantities to compare with experiments for predominantly 2D flows as indicated by Zabusky (1999). Figure 4 shows the evolution of the

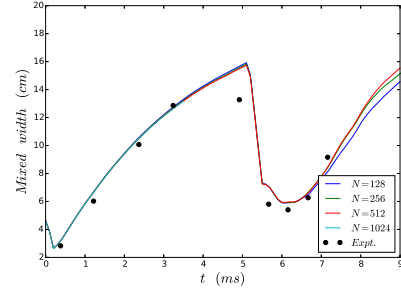


Figure 3: Comparison of the mixed width with experiments

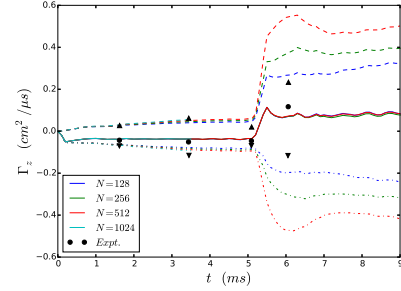


Figure 4: Comparison of the net circulation (solid), positive (dashed) and negative (dash-dot) contribution to the net circulation with experiments

net, positive and negative circulation. The net circulation converges with increasing grid resolution and compares well with the experiments. The positive and negative contributions to the circulation compare well with the experiments before reshock when the flow is predominantly 2D. After reshock, the positive and negative contributions to the circulation are not fully grid converged since the flow is highly 3D post reshock.

Turbulence Energy Budget

Using Favre averaging (Favre, 1969) and averaging in the homogeneous direction (z), a Turbulent Kinetic Energy (TKE) equation can be derived as (Chassaing *et al.*, 2013)

$$\begin{aligned} \frac{\partial \langle \rho \rangle \langle \tilde{K} \rangle}{\partial t} + \frac{\partial \langle \rho \rangle \langle \tilde{K} \rangle \langle \tilde{u}_j \rangle}{\partial x_j} = & - \frac{\partial \langle \rho \rangle \langle \tilde{K} u_j'' \rangle}{\partial x_j} - \langle \rho \rangle \langle \tilde{u}_i'' u_j'' \rangle \frac{\partial \langle \tilde{u}_i \rangle}{\partial x_j} \\ & - \frac{\partial \langle \rho \rangle \langle u_i'' \rangle}{\partial x_i} - \frac{\partial \langle \rho' u_i'' \rangle}{\partial x_i} + \langle \rho \rangle \frac{\partial u_i''}{\partial x_i} + \frac{\partial \langle \tau_{ij} u_i'' \rangle}{\partial x_j} - \langle \tau_{ij} \frac{\partial u_i''}{\partial x_j} \rangle \end{aligned} \quad (1)$$

where $\langle \cdot \rangle$ denotes simple Reynolds averaging and $\langle \cdot \rangle'$ is the corresponding fluctuation, $\langle \tilde{\cdot} \rangle$ denotes Favre averaging and $\langle \cdot \rangle''$ is the corresponding fluctuation. $K = \frac{1}{2} u_i'' u_j''$ is the instantaneous value of the TKE and its Favre averaged value is $\langle \tilde{K} \rangle = \frac{1}{2} \langle \tilde{u}_i'' u_j'' \rangle = \frac{1}{2} \langle \rho u_i'' u_j'' \rangle / \langle \rho \rangle$.

In a spatially integrated sense, the terms that are important for energetics are the shear production $-\langle \rho \rangle \langle \tilde{u}_i'' u_j'' \rangle \frac{\partial \langle \tilde{u}_i \rangle}{\partial x_j}$, turbulent dissipation $\langle \tau_{ij} \frac{\partial u_i''}{\partial x_j} \rangle$ and the pressure-dilatation correlation $\langle \rho \frac{\partial u_i''}{\partial x_i} \rangle$.

Figure 5a shows the spatially integrated shear production and turbulent dissipation as a function of time for different grid resolutions. Before reshock, we see that the production and dissipation grow slowly with time. Both production and dissipation peak

just after reshock around $t = 5.5ms$ and decay with time. After $t \approx 7.5ms$, we see a slow growth of the production due to shear caused by the large scale overturning of the interface. Figure 5a also shows that apart from the lowest resolution case (grid A), the integrated production and dissipation remain grid independent; the LAD terms indeed act like sub-grid models. Figures 5b and 5c show all the terms governing the integrated TKE evolution normalized by the TKE growth rate. To close the budget, we need to include the dissipation introduced by the dealiasing filter used in the simulations. However, we see that on grid C, the effect of the filter is smaller than all the other terms away from reshock and contributes to about 10% of the TKE budget. On grid D, the contribution of the filter falls to about 3%. Figures 5b and 5c also show that the pressure-dilatation correlation is important in the energetics and is comparable in magnitude to the turbulent dissipation.

Figure 6 shows the Reynolds stress anisotropy as a function of time. After the first shock interaction the state of turbulence is predominantly 1-component due to the anisotropy introduced by the shock interaction. After reshock, we see a move towards isotropy as the turbulence relaxes after compression by the shock. At larger times corresponding to the circulation time scale, we see a move away from isotropy due to the large scale shear. The inhomogeneity in this problem creates a competition between the two processes and consequently a non-monotonic return to isotropy.

Figure 7a shows the contours at $t = 6.5ms$ and Figure 7b shows the time evolution of the peak RMS turbulent Mach number of the flow $M_t = \sqrt{\langle u_i u_i \rangle} / c_s$ where c_s is the speed of sound. M_t is small before reshock but spikes at reshock becoming > 0.3 and decays rapidly. Post reshock, M_t asymptotes at ~ 0.1 which is not high enough for pressure-dilatation to play a significant role in the turbulence energetics. This is contrary to the fact that the pressure-dilatation correlation is significant even after the shock has traveled sufficiently far away from the interface as evidenced by the TKE budget. An inherent flaw with RANS type analysis for such a flow with a high degree of interaction between shocks and turbulence is that shocks that are not perfectly homogeneous in the averaging direction would contribute significantly to fluctuations that can be wrongly interpreted as turbulent features. Shocks can be expected to have some corrugation in the averaging direction as a consequence of interaction with the interface which does have strong variations in the homogeneous direction.

Scale decomposition

To clearly distinguish between the effect of shocks interacting with the turbulent mixing region and compressibility effects inherently present in the mixing region, we decompose the equations into large and small scales by an isotropic coarse-graining (or filtering) procedure. We follow the theoretical framework of Aluie (2013) to coarse-grain the equations using Favre filtering. As detailed in Aluie (2013), Favre filtering and defining the kinetic energy appropriately ensures that dissipation is isolated to the small scales and that energy injection is isolated to the large scales as is the case in incompressible turbulence. The kinetic energy above scales l are then governed by the following equation

$$\frac{\partial}{\partial t} \bar{\rho} \frac{|\bar{\mathbf{u}}|^2}{2} + \nabla \cdot \mathbf{J} = -\Pi - \Lambda + \bar{\rho} \nabla \cdot \bar{\mathbf{u}} - D_s \quad (2)$$

where \bar{f} is a filtered form of f and $\tilde{f} = \bar{\rho} \bar{f} / \bar{\rho}$ is the Favre filtered form of f . $\Pi = -\bar{\rho} \frac{\partial \tilde{u}_i}{\partial x_j} (\tilde{u}_i \tilde{u}_j - \tilde{u}_i \tilde{u}_j)$ is the production that transfers energy from large to small scales (if positive), $\Lambda = \frac{1}{\bar{\rho}} \frac{\partial \bar{p}}{\partial x_j} (\bar{\rho} \tilde{u}_j - \tilde{\rho}_j \tilde{u}_j)$ is the baropycnal work due to large scale pressure gradient acting on the small scale mass flux to transfer energy

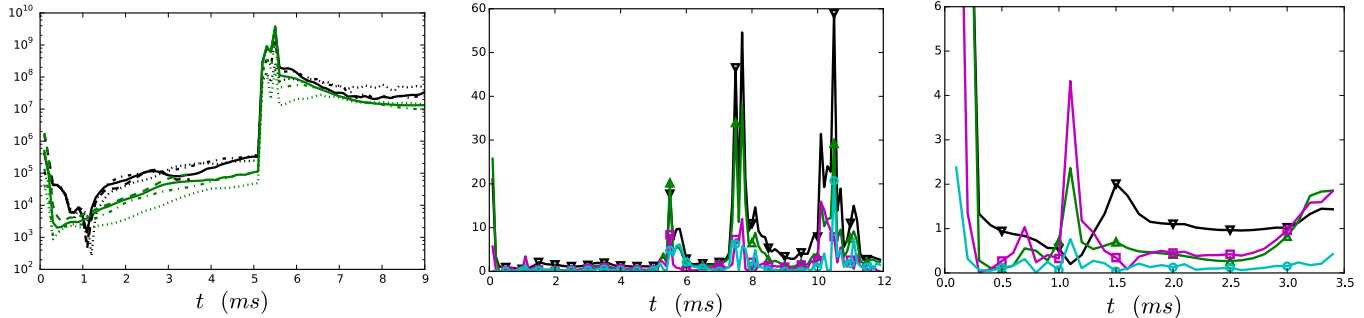
from large to small scales (if positive), $\bar{\rho} \nabla \cdot \bar{\mathbf{u}}$ is the pressure dilatation work acting on the large scales and $D_s = \frac{\partial \tilde{u}_i}{\partial x_j} \tilde{\tau}_{ij}$ is the dissipation acting on large scales.

We perform the coarse-graining using an isotropic Gaussian filter with a filter width of 4Δ where Δ is the grid spacing (Cook, 2007). To increase the filter width to $4n\Delta$, the same filter is recursively applied n^2 times.

Figures 9 and 10 show Π and Λ at $t = 7.2ms$ as a function of the filter width. At the largest filter widths, almost all the turbulence is sub-scale but as the filter width is reduced, a clear structure is seen in the plots of Π . The baropycnal work Λ reduces monotonically with decreasing filter width. As the filter width increases, more of the turbulence is unresolved and becomes a sub-scale mass flux that contributes to the baropycnal work. Note that Π and Λ are the only terms in Equation 2 that transfer energy from the large to the small scales and the sum of the two determines the energy flux from large to small scales. Figure 11 shows the large scale pressure-dilatation for different filter widths. This plot is revealing and shows the energy transfer mechanisms active in the flow. The large scale pressure dilatation is dominated by a rich and complex pattern of shockwaves and rarefactions and there is almost no correlation with the interfacial pattern visualized by the density in Figure 8. This indicates that it isn't the turbulence itself that is contributing to the compressibility effects but rather the pattern of shocks and rarefactions created by the inhomogeneity in the transverse direction during reshock that is continually interacting with the turbulent mixing region.

The sum $\int_{\Omega} \Pi d\Omega + \int_{\Omega} \Lambda d\Omega$ is the net energy transfer from scales larger than the filter width to those that are smaller. Assuming that energy is injected into the flow at time scales that are much larger than the time scales at which energy is cascaded to smaller scales (a quasi-steady state turbulence assumption), if $\int_{\Omega} \Pi d\Omega + \int_{\Omega} \Lambda d\Omega$ is independent of the scale of coarse-graining, then there is a conservative cascade of energy from large to small scales analogous to the Kolmogorov theory for incompressible turbulence. Figure 12 shows the energy transfer terms integrated over an interfacial region (same as the region shown in Figure 9 so that effect of the strong shocks are excluded) on a logarithmic scale as a function of the filter wavenumber $k_f = 2\pi/\lambda_f$ non-dimensionalized by the transverse domain length L_{yz} where λ_f is the filter width. Before reshock at $t = 3.5ms$, production at large scales is negative indicating that energy is transferred from the small scales to the large scales. The baropycnal work however, is higher than the production and is positive and hence the net energy flux to small scales is positive. Just after reshock at $t = 6.5ms$, production is positive across all scales and the baropycnal work is smaller but negative causing the net energy transfer to the smaller scales to be positive. $\int_{\Omega} \Pi d\Omega + \int_{\Omega} \Lambda d\Omega$ is also seen to be constant for the three highest wavenumbers indicating that the energy flux in scale is independent of the scale and an inertial range may be expected. Similar trends are seen at $t = 7.2ms$ with the main difference being that both production and baropycnal work are positive and transfer energy to small scales.

Figure 13 shows the same quantities as Figure 12 with the exception that the pressure dilatation term has the large scale subtracted out $\bar{\rho} \nabla \cdot \bar{\mathbf{u}} - \bar{\rho} \nabla \cdot \bar{\mathbf{u}}|_{k_f L_{yz} = 8\pi}$. The energy transfer terms are plotted on a linear scale. This highlights the variation of the pressure dilatation term with scale at the same order of magnitude as the rest of the terms. For all three times shown in Figure 13, we see that the pressure dilatation term does indeed have a scale dependence. Although shocks are highly localized in space, their effect on turbulence is broadband since in Fourier space, the spectrum of a shock decays as k^{-1} . This causes the broadband energy injection through the pressure-dilatation term. It must also be noted here that



(a) Integrated shear production (black) and turbulent dissipation (green) plotted against time. Dotted line is grid A, dashed-dotted line is grid B, solid line is grid C and dashed line is grid D. (b) Integrated shear production (black), turbulent dissipation (green), pressure-dilatation correlation (magenta) and filter dissipation (cyan) non-dimensionalized by the TKE growth rate on grid C. (c) Integrated shear production (black), turbulent dissipation (green), pressure-dilatation correlation (magenta) and filter dissipation (cyan) non-dimensionalized by the TKE growth rate on grid D.

Figure 5: Energetics and TKE budget based on the RANS equations.

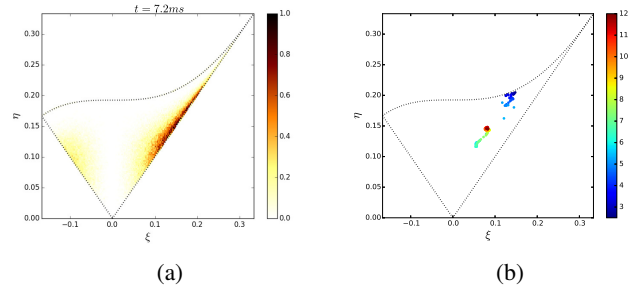
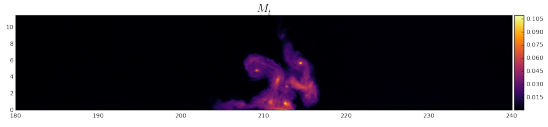


Figure 6: (a) Joint PDF of the Reynolds stress anisotropy at $t = 7.2ms$. (b) Evolution of the centroid of the joint PDF of Reynolds stress anisotropy (time represented by the colorbar).

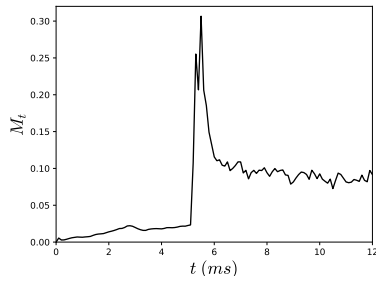
although the pressure dilatation varies with scale, the majority of its contribution comes from the very large scales as can be seen in Figure 12.

The integrated kinetic energy can be categorized into bins in wavenumber space so that the kinetic energy between k_f and $k_g > k_f$ may be defined as $K_{fg} = \bar{\rho} \frac{|u|^2}{2} \Big|_{k_g} - \bar{\rho} \frac{|u|^2}{2} \Big|_{k_f}$ to give an estimate of the scaling of the kinetic energy with wavenumber. In the inertial range, if the energy spectrum scales as $E(k) \propto k^\alpha$, $\alpha \neq -1$, then $K_{fg} \approx \int_{k_f}^{k_g} E(k) dk \propto k_{fg}^{\alpha+1} \left[\left(\frac{k_g}{k_f} \right)^{(\alpha+1)/2} - \left(\frac{k_g}{k_f} \right)^{-(\alpha+1)/2} \right]$ where $k_{fg} = \sqrt{k_f k_g}$. For constant $k_g/k_f (= 2$ here), we would expect an $\alpha + 1$ power law in the binned kinetic energy. For a $k^{-5/3}$ energy spectrum, we would expect a $k^{-2/3}$ scaling of the binned kinetic energy.

Figure 14 shows the binned kinetic energy at different times. Before reshock at 3.5ms, the flow is still transitional and not yet turbulent and hence the kinetic energy decays rapidly with wavenumber. At 6.5ms and 7.2ms when the flow is fully turbulent, we see a scaling close to k^{-1} which indicates that the kinetic energy spectrum $E(k)$ scales as k^{-2} . At both $t = 6.5ms$ and $t = 7.2ms$, we see a flattening of the binned kinetic energy at larger wavenumbers. This might indicate that at large scales, the time since reshock is insufficient to fully setup an energy cascade and that a larger range of scales is required in order to conclusively infer the kinetic energy scaling at higher wavenumbers.



(a) Plot of the RMS turbulent Mach number field M_t at $t = 6.5ms$.



(b) Turbulent Mach number M_t based on the RMS Reynolds fluctuating velocity plotted against time.

Figure 7: Turbulent Mach number M_t contours and peak as a function of time.

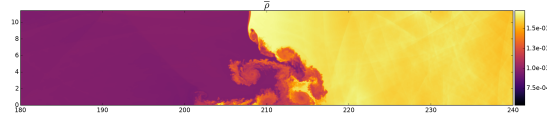


Figure 8: \bar{p} for filter width of 4Δ at $t = 7.2ms$

CONCLUSION

In this work, the inclined interface Richtmyer-Meshkov instability was simulated targeting the experiment of McFarland *et al.* (2014). The mixing width and circulation from the simulation compare well with those from the experiment. The energetics in the problem was investigated using a RANS type analysis and a scale decomposition analysis. A non-monotonic return to isotropy was seen post reshock due to the competing time scales of relaxation after compression of the turbulence by the shock and the circulation time scale. TKE budgets were presented for the RANS analysis and the effect of the dealiasing-filter was quantified and shown to be small ($\sim 10\%$). The RANS analysis showed that pressure-dilatation

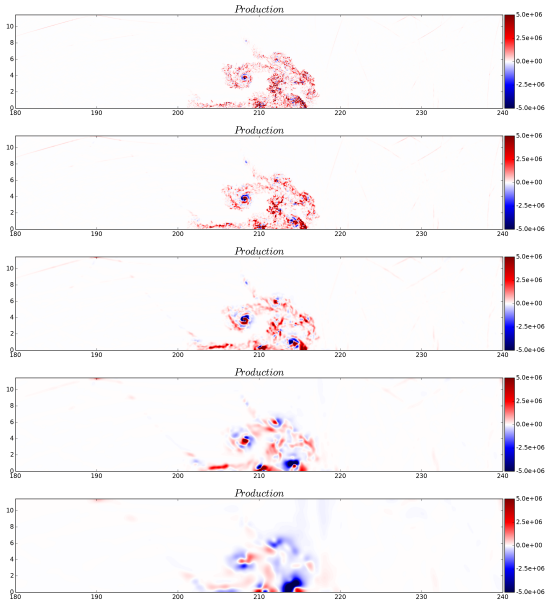


Figure 9: Π for increasingly larger filter widths at $t = 7.2ms$

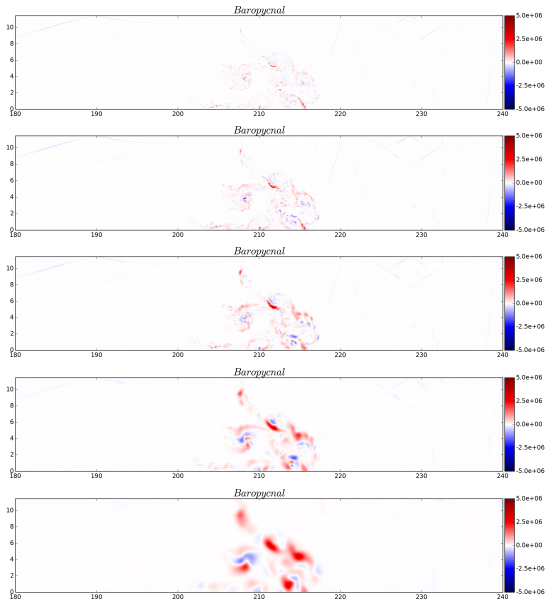


Figure 10: Λ for increasingly larger filter widths at $t = 7.2ms$

correlation was important but that the turbulent Mach number was relatively low (~ 0.1 RMS). Scale decomposition showed that the compressibility was due to a complex pattern of shocks and rarefactions created due to the inhomogeneity in the transverse direction and not due to compressible effects in the turbulent mixing region itself. Energetics were investigated at different scales and showed that the net flux of energy to smaller scales was scale invariant in the inertial range. Energy injected into the flow due to shocks and rarefactions was seen to be broadband. Finally, the kinetic energy was decomposed into bins in wavenumber space and a k^{-2} scaling of the energy spectrum was inferred although a larger range of scales could potentially reveal a different scaling at larger wavenumbers.

ACKNOWLEDGEMENTS

The authors would like to thank Dr. Andrew Cook for providing access to the Miranda code that was used for all the simulations

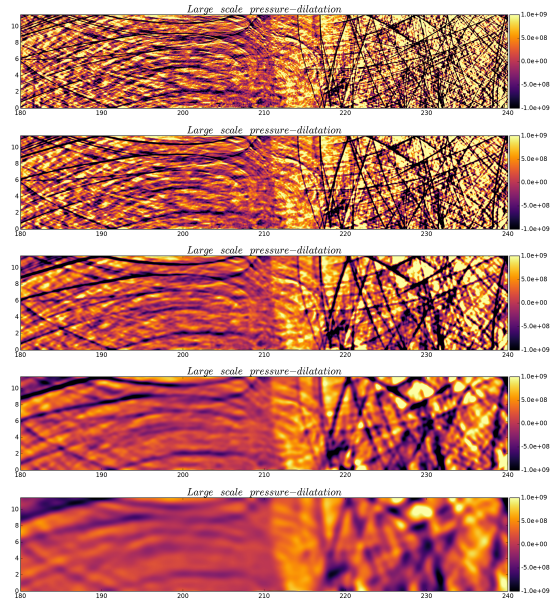


Figure 11: $\bar{p}\nabla \cdot \bar{u}$ for increasingly larger filter widths at $t = 7.2ms$

performed in this work.

This research is part of the Blue Waters sustained-petascale computing project, which is supported by the National Science Foundation (awards OCI-0725070 and ACI-1238993) and the state of Illinois. Blue Waters is a joint effort of the University of Illinois at Urbana-Champaign and its National Center for Supercomputing Applications. This work is also part of the ‘‘Shock-Induced Turbulent Multi-Material Mixing’’ PRAC allocation support by the National Science Foundation.

REFERENCES

- Aluie, Hussein 2013 Scale decomposition in compressible turbulence. *Physica D: Nonlinear Phenomena* **247** (1), 54–65.
- Chassaing, Patrick, Antonia, RA, Anselmet, Fabien, Joly, L & Sarkar, Sahotra 2013 *Variable density fluid turbulence*, vol. 69. Springer Science & Business Media.
- Cook, Andrew W 2007 Artificial fluid properties for large-eddy simulation of compressible turbulent mixing. *Physics of Fluids (1994-present)* **19** (5), 055103.
- Favre, A 1969 Statistical equations of turbulent gases. *Problems of hydrodynamics and continuum mechanics* pp. 231–266.
- Kawai, Soshi & Lele, Sanjiva K 2008 Localized artificial diffusivity scheme for discontinuity capturing on curvilinear meshes. *Journal of Computational Physics* **227** (22), 9498–9526.
- Kennedy, Christopher A, Carpenter, Mark H & Lewis, R Michael 2000 Low-storage, explicit runge–kutta schemes for the compressible navier–stokes equations. *Applied numerical mathematics* **35** (3), 177–219.
- Lele, Sanjiva K 1992 Compact finite difference schemes with spectral-like resolution. *Journal of computational physics* **103** (1), 16–42.
- McFarland, Jacob, Reilly, David, Creel, Skylar, McDonald, Christopher, Finn, Thomas & Ranjan, Devsh 2014 Experimental investigation of the inclined interface richtmyer–meshkov instability before and after reshock. *Experiments in fluids* **55** (1), 1–14.
- Tritschler, VK, Olson, BJ, Lele, SK, Hickel, Stefan, Hu, XY & Adams, Nikolaus Andreas 2014 On the richtmyer–meshkov in-

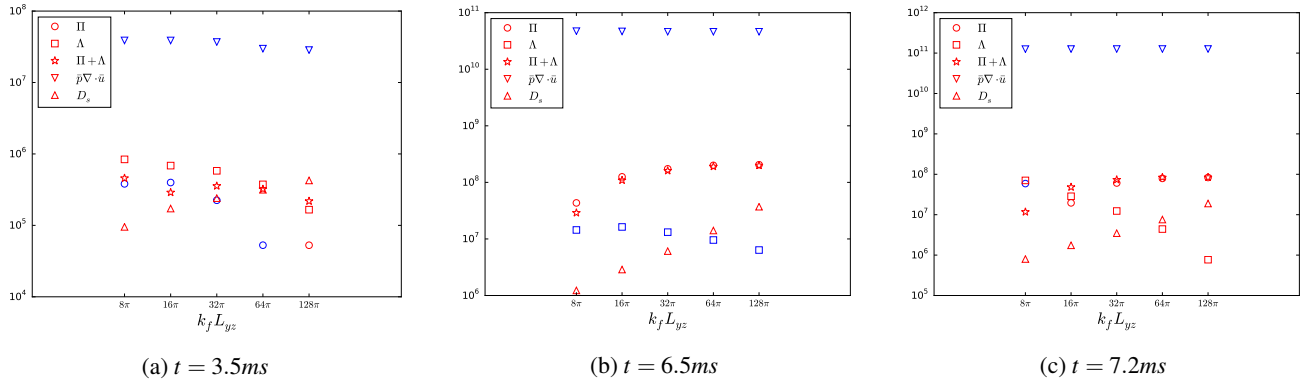


Figure 12: Plots of Π (circles), Λ (squares), $\Pi + \Lambda$ (stars), $\bar{p}\nabla \cdot \bar{\mathbf{u}}$ (triangles pointing down) and D_s (triangles pointing up) at different times. Red color indicates an energy sink in the large scale kinetic energy and blue color indicates an energy source.

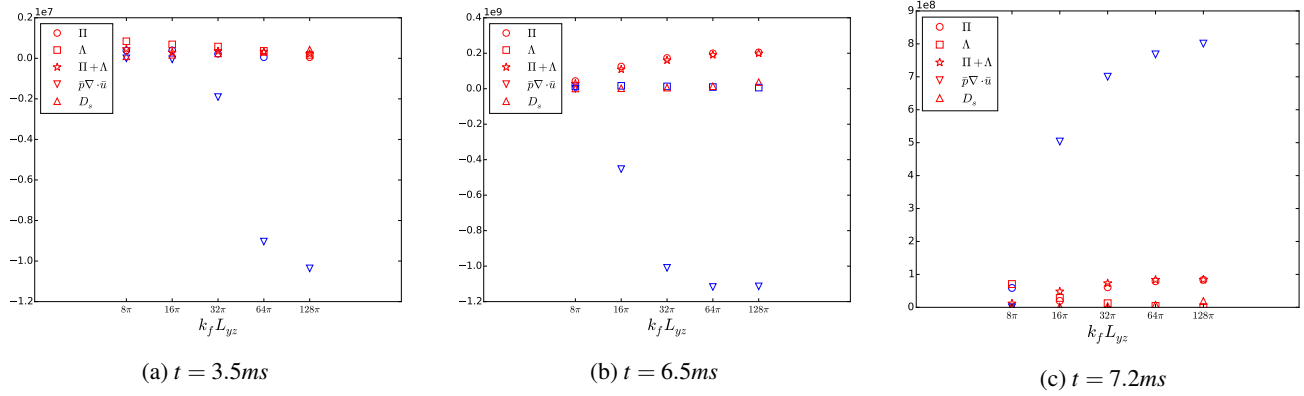


Figure 13: Plots of Π (circles), Λ (squares), $\Pi + \Lambda$ (stars), $\bar{p}\nabla \cdot \bar{\mathbf{u}} - \bar{p}\nabla \cdot \bar{\mathbf{u}}|_{k_f L_{yz}=8\pi}$ (triangles pointing down) and D_s (triangles pointing up) at different times. Red color indicates an energy sink in the large scale kinetic energy and blue color indicates an energy source.

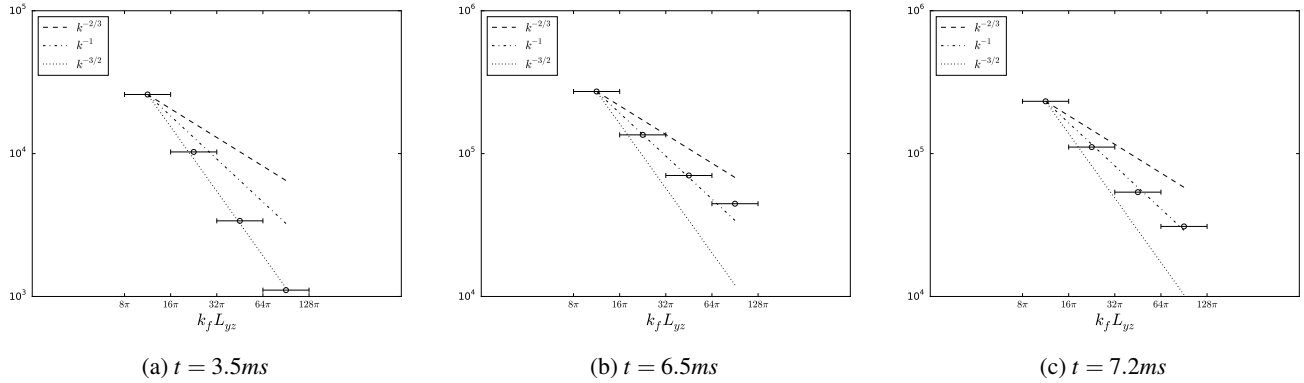


Figure 14: Plots of the kinetic energy in scale intervals depicted by the horizontal bars at different times. Symbols are the data. Dashed line indicates a $-2/3$ power law, dashed-dotted line indicates a -1 power law and dashed line indicates a $-3/2$ power law.

stability evolving from a deterministic multimode planar interface. *Journal of Fluid Mechanics* **755**, 429–462.
Zabusky, Norman J 1999 Vortex paradigm for accelerated in-

homogeneous flows: Visiometrics for the rayleigh-taylor and richtmyer-meshkov environments. *Annual review of fluid mechanics* **31** (1), 495–536.